Mechanical properties of soot particles: the impact of crosslinked polycyclic aromatic hydrocarbons

Laura Pascazio[1], Jacob W. Martin[1,2], Maria L. Botero[3], Mariano Sirignano[4], Andrea D'Anna[4], Markus Kraft[1,2,5]

[1]Department of Chemical Engineering and Biotechnology, University of Cambridge, West Site, Philippa Fawcett Drive, Cambridge CB3 0AS, UK

[2]Cambridge Centre for Advanced Research and Education in Singapore (CARES) CREATE Tower, 1 Create Way, Singapore, 138602

[3]Department of Mechanical Engineering, National University of Singapore 9 Engineering Drive, Singapore, 117576

[4]Dipartimento di Ingegneria Chimica, dei Materiali e della Produzione Industriale, Università degli Studi di Napoli Federico II Piazzale V. Tecchio 80, Napoli, 80125, Italy

[5]School of Chemical and Biomedical Engineering, Nanyang Technological University 62 Nanyang Drive, Singapore, 637459

[1]Corresponding Author: e-mail: mk306@cam.ac.uk

Abstract

In this paper, we estimate the degree of crosslinking within soot particles making use of reactive molecular dynamics simulations of mechanical properties of crosslinked polycyclic aromatic hydrocarbons (PAH). Representative systems of PAH (pyrene, coronene, ovalene and circumpyrene) with a density similar to soot and with varying degrees of crosslinking were built. Uniaxial tensile test simulations were carried out on the systems and the yield stress of each sample was calculated. The hardness was estimated from the yield stress using an empirical conversion constant and the obtained values were compared with nanoindentation experiments of soot particles. The results show that mature ethylene and diesel soot particles are expected to present a degree of crosslinking between $2.1 - 3.0$ and $3.0 - 3.5$, respectively, to have a value comparable to the hardness found experimentally. Finally, an MD simulation of nanoindentation of a particle of crosslinked coronene molecules provided an alternative means to compute the empirical constant used to convert the yield stress in hardness. These results reveal the importance of crosslinking reactions during soot maturation that give rise to a structure in which the majority of aromatics are aliphatically-linked in a 3D network.

1 Introduction

Carbonaceous particles produced during combustion present a pressing problem to human health and the climate (McConnell et al., 2007; Bond et al., 2013; Landrigan et al., 2017), but can also produce many novel carbon materials used as pigments, reinforcing rubbers and battery anodes (Wang, 2011). Both goals - destroying soot and controlling the synthesis of carbon black - require an understanding of the chemistry and morphology of carbon particles.

The complexity of the soot nucleation process makes its study challenging experimentally and computationally. Polycyclic aromatic hydrocarbons (PAH) are widely accepted as precursors of soot particles (Wang, 2011; Frenklach, 2002; Dobbins et al., 1998; D'Anna, 2009). Three primary pathways have been postulated for the soot nucleation and growth processes (Wang, 2011). The first one involves the growth of "two-dimensional" PAH into curved, fullerene-like structures (Homann, 1998), the second one involves the physical dimerisation of planar PAH and their coalescence into clusters of stacked PAH (Frenklach and Wang, 1991; Herdman and Miller, 2008; Schuetz and Frenklach, 2002) and the third one is a chemical pathway in which PAH react to form crosslinked three-dimensional structures (D'Anna et al., 2001; Violi et al., 2002, 2004; Ciajolo et al., 2000; Commodo et al., 2015, 2019). All the above mechanisms are believed to take part in the soot formation process, but their relative importance or feasibility at different conditions and temperatures is still unclear. Previous studies utilising different atomic simulation methods, such as density functional theory (Zhang et al., 2014), molecular dynamics (MD) (Schuetz and Frenklach, 2002; Totton et al., 2012, 2010; Chung and Violi, 2011; Iavarone et al., 2017; Pascazio et al., 2017; Mao et al., 2017, 2018), Monte Carlo (Rapacioli et al., 2005) and well-tempered metadynamics simulations (Elvati and Violi, 2018, 2013) have shown that the physical interactions between medium-sized PAH are not strong enough to stabilise clusters at high temperatures, and only aromatic molecules as big as circumcoronene are able to cluster at temperatures where soot forms ($\approx$1500 K). Understanding the degree of

crosslinking in soot particles could then be important for determining which mechanisms are involved in their growth and potentially help in understanding their inception process.

From an experimental perspective, the primary particles (10–50 nm) making up soot aggregates are known to consist of aromatic layers with some degree of ordering often referred to as basic structural units (Alfè et al., 2009). Early models of carbon black and soot proposed a homogeneous distribution of these structural units throughout the primary particles (Sweitzer and Heller, 1956). However, the advent of electron microscopy has revealed an internal structure to these particles, indicating a core-shell structure with less structured nuclei inside of carbon black (Donnet et al., 1968; Heckman and Harling, 1966; Heidenreich et al., 1968) and potentially multiple nuclei (Ishiguro et al., 1997). The development of a core-shell structure has been correlated with the maturity of the particle, with the H/C ratio and band gap decreasing with height above the burner (Kholghy et al., 2016; Dastanpour et al., 2017; Commodo et al., 2015; Minutolo et al., 1996; Tregrossi and Ciajolo, 2010; Russo et al., 2013; Miller et al., 2013). High resolution transmission electron microscopy (HRTEM) images also showed fringe lengths increasing and interplanar distances decreasing with soot maturity and the flame temperature (Alfè et al., 2009; Kholghy et al., 2016; Alfè et al., 2010; Apicella et al., 2015). These observations have been interpreted as an indication that carbonisation processes are occurring from the outside in, which could impact the reactivity of these particles as well as the gas phase chemistry by evolving hydrogen (Heckman and Harling, 1966; Sediako et al., 2017).

Carbonisation of PAH is known to occur through a radical mechanism in which an aliphatic crosslink is initially formed, followed by dehydrogenation and ring formation (cyclodehydrogenation) (Lewis, 1980; Talyzin et al., 2011; Unterreiner et al., 2004). While imaging these crosslinks directly in soot particles has been difficult, nanoindentation suggests significant crosslinks when compared with non-crosslinked nanocrystalline graphite, which has yet to feature prominently in discussions of soot and carbon black (Bhowmick and Biswas, 2011; Bhowmick et al., 2011). Nanoindentation measures the force as a well-defined tip is pushed into a material from which the hardness (H) can be determined –

4

$H = P_{max}/A_c$ where P_{max} is the maximum load and A_c is the indentation area. Table 1 summarises the findings from nanoindentation studies of various carbon materials.

[Table 1 about here.]

The relative hardness of different carbon materials can provide an indicator for the degree of crosslinking. Nanocrystalline graphite is known to be an un-crosslinked structure made of mobile graphene sheets with a very low hardness (0.1–0.4 GPa). Nanoindentation studies of amorphous carbon film containing crosslinked nanocrystalline graphite clusters indicate that hardness increases with sp^3 bond content in the structure (Fan et al., 2013). Looking at the hardness values of mature soot and carbon black, values closer to a hard crosslinked carbon such as charcoal are found. These results indicate that mature soot and carbon black are probably carbonised and crosslinked and are not van der Waals solids. This is also supported by chromatography where soot extracted in a fuel-rich premixed ethylene flame contains an initially eluted fraction with PAH of masses 300–600 m/z, determined from laser desorption time of flight mass spectrometry and a secondary peak of polymerised products, matching that of pitch made from polymerised naphthalene (Alfè et al., 2008). These results support the idea of carbonisation beginning with single aliphatic bonds forming between aromatic molecules.

The purpose of the present study is therefore to consider and estimate the degree of crosslinking in soot particles. We do this by studying the mechanical properties of an idealised structure of soot described by crosslinked PAH using the methodology reported in section 2. In section 3 we detail the construction of the crosslinked PAH structures. In section 4 we performed reactive force field MD simulations and computed stress-strain curves of such structures as well as their yield stress. In section 5 the hardness of systems with varying degrees of crosslinking was calculated and the degree of crosslinking within soot particles was estimated, and our results compared to the hardness found from nanoindentation experiments of soot. Finally, in section 6 we performed an MD simulation of a particle of crosslinked PAH being nanoindented with a degree of crosslinking in the range

found for soot.

2 Methodology

MD was employed to simulate the uniaxial tensile deformation of crosslinked PAH structures, in order to investigate the effect of the degree of crosslinking in the structure on its mechanical properties. To achieve this goal the following procedure was adopted:

1. A crosslinking procedure was developed to build PAH boxes with varying degrees of crosslinking.

2. MD simulations of uniaxial tensile deformation were carried out on the selected structure and their yield stresses and Young's moduli were evaluated as a function of the degree of crosslinking in the structure.

3. The yield stress was converted to hardness using an empirical conversion constant obtained assuming that the crosslinked PAH structures have an intermediate structure between HOPG and diamond. Then the obtained hardness values were compared with experimental nanoindentation hardness data.

4. The comparability of hardness values obtained using this method and experimental nanoindentation hardness values was assessed by performing an additional MD simulation of nanoindentation of a particle of crosslinked PAH with a degree of crosslinking in the range found for soot.

Every part will be described in detail in the following sections. A schematic diagram of the adopted methodology is reported in Figure 1.

[Figure 1 about here.]

The reactive force field MD simulations were carried out using the LAMMPS software (Plimpton, 1995). Pyrene ($C_{16}H_{10}$), coronene ($C_{24}H_{12}$), ovalene ($C_{32}H_{14}$) and circumpyrene ($C_{42}H_{16}$) (Figure 2) were chosen as starting monomers, since they span the size

range of fragments found in soot particles (Botero et al., 2016). The interactions within molecules were modelled using an updated version of the adaptive intermolecular reactive empirical bond order (AIREBO) potential (Stuart et al., 2000), known as AIREBO-M (O'Connor et al., 2015), which has been widely used to investigate the mechanical and thermal properties of carbon-based nanomaterials. AIREBO-M uses the same functional form as the hydrocarbon second-generation REBO potential (Brenner et al., 2002), with an additional Morse term to represent the van der Waals interactions. The Morse potential replaces the Lennard-Jones potential used in the original AIREBO, which has been shown to yield unphysical results for carbon systems subjected to high pressures (O'Connor et al., 2015). The Morse potentials are parameterised by high-quality quantum chemistry calculations and do not diverge as quickly as the Lennard-Jones potentials when particle density increases. This allows AIREBO-M to retain accuracy to much higher material densities than AIREBO. A force field benchmark is reported in the Appendix A.1.

[Figure 2 about here.]

3   Generation of crosslinked structures

The construction of the crosslinked structure was realised as follows:

1. Homomolecular systems of pyrene, coronene and ovalene molecules and a hetero-molecular system of four different PAH molecules (pyrene, coronene, ovalene and circumpyrene) were built. The heterogeneous system is composed of 25% in number of each considered PAH.

   Monomers were randomly placed in a cubic simulation box using the PACKMOL software (Martinez et al., 2009) (step 1 in Figure 1). The number of molecules was chosen in order to generate a starting cubic box with side length 43 Å and a density of 1.5 g/cm^3, which is a commonly assumed value for soot particles (Zhao et al., 2007). This value is slightly lower than the mature soot density value (1.8 g/cm^3);

higher density systems have also been reported for comparison in Appendix A.4. The initial un-crosslinked structure was first minimised and then equilibrated for 200 ps in the isothermal and isochoric ensemble (NVT) at 300 K with a corresponding integration time step of 0.5 fs and maintaining periodic boundary conditions. A constant temperature was controlled by the Berendsen thermostat, with a time constant of 0.1 ps. Due to the periodic boundary conditions, covalent bonds can form not only between the monomers inside the simulation cell, but also between monomers across the periodic boundaries. To have accurate results, it is necessary to have a homogeneous crosslinking density in all the simulation box. It was verified that with shorter equilibration time the molecular distribution across the boundary is affected and the crosslink density in the boundary region is lower compared to the density in the central region such that, during the tensile test, the structure fails near the boundaries and the tensile test results are in error.

2. The crosslinking process starts with hydrogen removal and consequent bond creation between molecules. Reactive sites were created in the simulation boxes by directly removing hydrogen atoms from every second carbon atom around the rim of the molecule (step 2 in Figure 1). The use of a reactive potential allows for chemical bond formation to occur between a pair of reactive sites. The choice of removing alternating H atoms from the molecule rim avoids ring condensation between monomers due to the presence of the neighbouring hydrogen atoms and only allows the production of aliphatic links between two aromatic molecules. The types of crosslinks formed were the most preliminary types of crosslinks where a single aliphatic linkage joins two pericondensed aromatic molecules (Lewis, 1980; Unterreiner et al., 2004). Single crosslinks between planar PAH cause the two aromatic planes to be non-parallel due to the steric interactions between the neighbouring hydrogen atoms and allows for 3D crosslinking to occur. Ring condensation events owing to H abstraction from a carbon atoms next to a reactive site are still possible. A structural assessment was

conducted to check the occurrence of other possible reactions (i.e. ring condensation, H abstraction or migration and ring opening) and it is reported in Appendix A.5.

3. Reactive force field simulations in the NVT ensemble were run and halted after different simulation durations to provide varying degrees of crosslinking (step 3 in Figure 1). The degree of cross-linking (CL) was defined as:

$$CL = \frac{2 \cdot \text{number of crosslinks in the system}}{\text{number of starting monomers}}. \tag{1}$$

By definition, CL represents the average number of crosslinks present within each molecule in the system. It means that, when the CL density is 1, each molecule has on average a single crosslink and mainly dimers are formed. A CL density of 2 is required for a polymer where on average each molecule has two crosslinks and a CL density between 2 and 3 is required for a 3D network.

A time step of 0.25 fs was adopted for the integration of the atomic equations of motion and the Berendsen thermostat was used to maintain a constant temperature of 1000 K with a time constant of 0.1 ps. These simulation parameters ensured a stable simulation as significant heat had to be removed due to bond formation. The simulation time was set to 100 ps.

4. Hydrogens were then added back to the sites that had not formed crosslinks (step 4 in Figure 1). Then an energy minimisation was conducted on the system.

Although the methodology adopted is practical and quick for our purpose, it is important to highlight that these simulations cannot be related to a chemically realistic mechanism for a crosslinking process. This process has been adopted only to obtain starting geometries with varying degrees of crosslinking. This scheme allows structures to be rapidly formed through an unphysical scheme that provides a suitable geometry matching an experimental system (Thompson et al., 2017). Moreover, such a procedure requires rapid heat removal and therefore strongly coupled thermostats were used, such as the

Berendsen thermostat (Ranganathan et al., 2017). While the Berendsen thermostat does not allow equilibrium properties to be accurately sampled, it is suitable for producing the starting configurations for the tensile tests.

The degree of crosslinking (CL, Eq. 1) is reported in Figure 3 as a function of the simulation time. Initially there were numerous reactive sites available for the crosslinking reaction, which contributed to a rapid increase in the degree of crosslinking in the first picoseconds of simulation. As the reaction proceeded, fewer reactive sites were available for the crosslinking reaction and thus, the curve approaches a value between 3.5 and 4 in all three systems. Considering the computational cost and a limited improvement in terms of the crosslinking degree, the current simulation time (100 ps) can be considered reasonable. An increase in CL can be also translated in a decrease in the H/C ratio. The investigated systems have an H/C ratio that goes from 0.625 (uncrosslinked pyrene) to 0.32 (crosslinked ovalene) (Table 2). The experimental H/C value of soot goes from 0.6 (young soot) to $\approx$ 0.2–0.1 (mature soot) (Russo et al., 2015). The generated structures are then representative of soot at all stages of its formation because of the wide range of H/C ratio and PAH sizes considered. Although our samples did not reach the H/C value of mature soot, a further decrease can be attributed to a consequent carbonisation process that follows crosslinking reactions as discussed in the next section.

[Figure 3 about here.]

4   Molecular dynamics simulations of uniaxial tensile deformation

Reactive MD simulations were used to characterise the mechanical responses of the systems. Uniaxial tensile loading was applied on selected configurations with varying degrees of crosslinking obtained during the crosslinking procedure along the x-direction with a time step of 1 fs, while the y and z boundaries were controlled using the NPT equations of motion to maintain atmospheric pressure (step 5 in Figure 1). The tensile properties are dependent on the strain rate adopted in the simulation, making it crucial that a low

enough value is selected to have consistent results. A strain rate of $5 \cdot 10^8\ s^{-1}$ was used for all of the simulations. This choice for the parameter comes from a sensitivity analysis reported in Appendix A.2 in which four different strain rate were tested ($1 \cdot 10^{10}\ s^{-1}$, $5 \cdot 10^9\ s^{-1}$, $1 \cdot 10^9\ s^{-1}$ and $5 \cdot 10^8\ s^{-1}$). It was also verified that uniaxial tensile tests deforming in y and z directions give almost the same results due to the isotropic behaviour of the process. Periodic boundary conditions were applied to the simulation box to avoid edge effects. The environmental temperature was maintained at 300 K by using the Nosé-Hoover chains thermostat with three chains (Martyna et al., 1992). For barostating, the Parrinello-Rahman barostat was used (Parrinello and Rahman, 1981). This combination accurately reproduced the dynamics of an NPT ensemble and is widely used for tensile tests with many studies published in the last years using such a procedure (Chang et al., 2017; Shahini et al., 2017; Zhang and Zhou, 2018; de Tomas et al., 2018). Prior to loading, the system was simulated in the NPT ensemble (300 K, 1 atm) for 400 ps to relax the system after the crosslinking procedure and make the temperature, pressure, and other properties steady before deformation. The time step used was 1 fs and a Nosè-Hoover thermostat and a Parrinello-Rahman barostat were applied to control the system temperature and pressure during the equilibration step with a time constant of 0.1 ps. Although the starting box expanded until it reached atmospheric pressure at the desired temperature, the density remained almost the same at the end of the equilibration step.

The resulting stress-strain curves were plotted and the yield stresses for the different samples were determined.

[Figure 4 about here.]

Figure 4 shows stress versus strain curves for these PAH structures with varying degrees of crosslinking. All of the structures show a J-shaped stress-strain curve, where initially small increases in stress give large extensions, however, at larger extensions the material becomes stiffer and more difficult to extend, requiring a larger increase in the stress to obtain the same strain increment. This strain hardening behaviour is typical of

materials that present chains in their structure, such as biological materials and polymers (Mitsuhashi et al., 2018; Takano and Koibuchi, 2017) and has been seen in carbon fibres during carbonisation (Li et al., 2017).

The simulation results indicate that the tensile property increases with the degree of crosslinking. The crosslinking reactions change some physical interactions to covalent bonds, which strengthens the mechanical properties of the sample. It is interesting to note that the tensile property of the un-crosslinked structure ($CL = 0$), *i.e.* when monomers interacting only through physical interactions, is very low (order of MPa).

The yield point is defined as the stress at which a material begins to deform plastically. To identify the precise location of the yield point, the methodology proposed by Qomi et al. (Qomi et al., 2017) was used, in which a numerical unloading procedure was performed at different locations along the loading path. The failure was assigned to the last point that exhibits reversible behavior on the stress-strain curve and hence does not lead to residual stress at zero strain (step 6 in Figure 1). In Figure 5, three loading-unloading paths for the coronene system with $CL = 3.75$ are reported as an example.

[Figure 5 about here.]

The unloading paths from point 1 and 2 lead to residual stress at zero strain, indicating that the material deformed plastically during the loading process. The unloading from point 3 goes back to the original configuration with no residual stress. Therefore, point 3 was assigned as the yield point in that system, because a slight perturbation from point 3 will incur an irreversible deformation in the structure.

The yield stresses (σ_f) obtained by the load-unload procedure for all the systems investigated are shown in Figure 4 (red circles) and reported in Table 2. The strain at the yield point decreases with increasing degrees of crosslinking in the structure, as expected. This is due to decreased mobility of the structural units since the material becomes more tightly bonded as the CL density increases. Similar considerations can be made for the concave up behaviour of the stress-strain curves that is nearly lost at high CL.

5 Hardness and Young's modulus

It is not possible to compare the simulated yield stress directly to experimental data because it is not possible to perform tensile test experiments on soot nanoparticles. However, it is possible to determine experimental measurements of soot particle hardness using nanoindentation techniques (Bhowmick and Biswas, 2011; Bhowmick et al., 2011; Jenei et al., 2018). For many classes of materials such as metals (Tabor, 1951) and several polymers (Flores et al., 2000), a linear relationship is observed between the indentation hardness (H) and the yield stress (σ_f)

$$H = K\sigma_f, \tag{2}$$

where K is an empirical constant. Under the assumption that soot nanoparticles obey a linear relationship of the form shown in Eq. (2) and given a suitable value of K, the simulated yield stress can be used to calculate a value of the hardness.

In this work we make the additional assumption that a suitable value of K can be estimated as the average of the values of K for highly oriented pyrolytic graphite (HOPG) and diamond. This assumption is made on the basis that crosslinked PAH structures have both in-plane and out-of-plane PAH crosslinks, such that they have an intermediate structure between that of HOPG and diamond. The yield stress values for diamond and HOPG were obtained using the same uniaxial tensile simulation conditions. Hardness values were taken from Table 1 and the corresponding K values were calculated using Eq. 2. The empirical conversion constant K was found to be 1.2 for diamond and 1.6 for HOPG, so $K = 1.4$ was chosen for the PAH crosslinked structures.

Having estimated a value for K, the simulated yield stresses were used to calculate the hardness of crosslinked PAH structures as a function of the degree of crosslinking using Eq. 2. The appropriateness of the methodology used to calculate the hardness was assessed by performing a nanoindentation simulation to directly estimate the hardness of a particle of

crosslinked PAH (see Section 6).

The calculated hardness is reported in Table 2 and plotted as a function of the degree of crosslinking in the structure in Figure 6a. The hardness grows with the degree of crosslinking in the structure.

[Figure 6 about here.]

[Table 2 about here.]

The crosslinking enhances the mechanical properties of the material tested. There is a weak dependence on the size of the aromatic molecule used as the monomer. For a fixed degree of crosslinking, the pyrene systems provide a lower hardness value compared to the coronene and ovalene systems, indicating that the physical interactions influence, even if only slightly, the mechanical properties. However, moving from coronene to ovalene, the difference between the two curves becomes smaller, suggesting that the physical interactions of molecules of sizes greater than or equal to coronene provide similar contributions to the hardness value. The heterogeneous system was found to yield similar hardness values compared to the homogeneous systems.

These results clearly show that the mature soot structure must contain crosslinks between its constituent molecules to have a hardness value comparable to that found experimentally by Bhowmick et al. (Table 1). The presence of crosslinks in mature soot particles suggests that the conversion of soot precursor particles to mature soot particles in flames involves a crosslinking process. This process is likely followed by a carbonisation process, in which ring condensation of PAH occurs after the formation of an aliphatic crosslink and a subsequent dehydrogenation reaction leads to a new ring forming (Lewis, 1980; Talyzin et al., 2011; Unterreiner et al., 2004). HRTEM studies have shown that fringe lengths increase and interplanar distances decrease with increased soot maturity and flame temperature (Alfè et al., 2009; Kholghy et al., 2016; Alfè et al., 2010; Apicella et al., 2015). In the carbonisation of pitch (Lewis, 1980; Buseck et al., 1987), the lengthening of the fringes is considered to be primarily due to these structures. In the same way, the lengthening of

14

the fringes in soot particles indicates carbonisation. The subsequent ring formation aligns the two aromatic planes and produces a single planar PAH molecule. The lack of sensitivity between the PAH size on the hardness-crosslink relationship suggests that the results would not be significantly affected by a further increase in the PAH size, i.e the lengthening of the fringes due to the carbonisation process. The results also give information on the degree of crosslinking in soot particles prepared in different combustion environments - $CL = 2.1 - 3.0$ for ethylene soot and $CL = 3.0 - 3.5$ for diesel soot (Figure 6a) - indicating that crosslinking reactions play a different role at different conditions.

The Young's modulus (Y) was also calculated as the slope of the linear part of the stress-strain curve and is reported in Table 2. The slopes of the curves increase with increasing degree of crosslinking for all the investigated systems, which implies that the Young's modulus increases with increasing crosslink density. Figure 6b shows the linear dependence of Y from CL and how the values arrange along the same line independently from the starting monomer. The results are in good agreement with the results reported by Jenei et al. in which diesel soot particles showed an average hardness value of 4.9 GPa and an average Young's modulus of 8.2 GPa, both values corresponding to a $CL \approx 2.5$ in our simulations (Jenei et al., 2018). The linear dependence of the hardness and Young's modulus on CL indicate that every crosslink present in the structure contributes to the mechanical properties and elastic behaviour of the structure, resulting in a direct proportionality between them.

Finally, systems with a low CL were obtained by starting from a lower number of reactive sites in the crosslinking procedure for the coronene case as explained in Appendix A.3. Figure 7 shows the hardness as a function of the degree of crosslinking for all the coronene systems.

[Figure 7 about here.]

The ability of a material to extend longitudinally is related directly to its molecular mobility. Considering the obtained curve, we can distinguish three regions characterised

by a different molecular mobility:

1. $CL < 1$: The systems present hardness values of the order of MPa and they can be considered as 'soft' materials. This CL corresponds to molecules with a single crosslink on average and hence mainly products of chemical dimerisation are formed. As a consequence of the very high molecular mobility and the dominance of physical interactions between molecules, we can assume that at flame temperature ($>$1000 K) they would show a liquid-like behaviour.

2. $1 < CL < 1.5$: The material hardness in this region starts to increase nonlinearly, going from values of order of MPa to the order of GPa. As soon as the crosslinking degree increases a 3D network starts to form in the structure.

3. $CL > 1.5$: The hardness increases linearly with CL and the systems present hardness values of the order of GPa (hard materials). The structure starts to be tightly bonded and the molecular mobility decreases.

These latter results might explain the transition from the liquid-like behaviour of incipient soot particles to the solid state (mature soot) at flame temperatures as an increase in the crosslinking density. Due to the lack of nanoindentation experiments conducted on incipient soot particles, the degree of crosslinking cannot be estimated for incipient soot as we did for mature soot. Although there is no direct evidence of crosslinking in the early stages of soot formation, our results do not exclude it. In fact, as reported in Figure 7, a degree of crosslinking higher than approximately 1.5 is required to have a hardness value of the order of GPa. So early soot particles, characterised by a liquid-like behaviour, can have a degree of crosslinking higher than 0.0 and lower than 1.5 (the range corresponding to a chemical dimerisation) and still behave as a liquid at high temperatures. Nanoindentation experiments on incipient soot particles could provide insight into whether they are liquid like (un-crosslinked) or carbonised (crosslinked) and when this transition occurs.

6 Molecular dynamics simulation of nanoindentation

To convert the yield stress values into hardness, an empirical conversion constant $K = 1.4$ was used in the previous section, assuming that crosslinked PAH structures have an intermediate structure between highly oriented pyrolytic graphite (HOPG) and diamond. The impossibilities of performing a tensile test experiment on a soot particle leaves uncertainties on the K value and hence on the calculated hardness that is dependent on this value. To confirm the assumptions made, a molecular dynamics simulation of nanoindentation was performed to assess the consistency of the hardness values calculated from the simulated yield stresses (see Section 5) with hardness values estimated directly from nanoindentation simulations. While the uniaxial tensile test simulations are computationally cheap, nanoindentation simulations are expensive and so were only performed for a single particle.

Nanoindentation was simulated for a spherical particle with a diameter of 7 nm and density of 1.5 g/cm³, composed of crosslinked coronene molecules with $CL = 3$ (a value in the range found for soot particles in the previous section). The crosslinks between the coronene molecules were created through the same crosslinking procedure described in section 3 (steps 2, 3 and 4). The PACKMOL software was used to create the spherical starting configuration for the crosslinking process. Due to the high simulation temperature, a position potential was implemented during the reactive force field MD simulation (step 3) to reach the desired degree of crosslinking without the loss of molecules from the particle. This potential acted on molecules located at the particle boundary to restrain them within a spherical volume. The simulation was then stopped at the desired degree of crosslinking in the same manner as the periodic simulations.

The particles were then relaxed at 300 K for 100 ps in the NVT ensamble using the Nosé–Hoover chains thermostat with three chains. During this step, the position potential adopted previously was removed and the result was a nearly spherical particle.

Once equilibrated, the nanoparticle was subjected to indentation. The setup for the nanoindentation simulations is shown in Figure 8. The atoms were kept at a constant

17

temperature by a Nosé-Hoover thermostat. The time step was set to 0.5 fs. A virtual wall was placed at the bottom of the particle. The indentation simulations were performed with a planar indenter initially placed at 5 Å above the particle which moves at a constant speed of 25 m/s during the loading and unloading stages up to a maximum indentation depth of 60% of the particle diameter.

[Figure 8 about here.]

The load-displacement curve is reported in Figure 9. The hardness of the particle is calculated as follows:

$$H = \frac{P_{max}}{A_c} \tag{3}$$

where P_{max} is the maximum force acting on the indenter at the end of the loading stages and A_c is the contact area. The resulting hardness is 5.2 GPa. This value is consistent with the results obtained from the uniaxial tensile test simulations (insert in Figure 9), confirming that the K value range used for calculating the hardness from the yield stress is appropriate.

[Figure 9 about here.]

7   Conclusions

The degree of crosslinking in soot particles was explored using reactive MD uniaxial tensile simulations of idealised soot structures described by crosslinked PAH. Homomolecular systems of pyrene, coronene and ovalene molecules and a heteromolecular system of four different PAH (pyrene, coronene, ovalene and circumpyrene) with densities similar to soot and with varying degrees of crosslinking were built. The yield stress of each structure was calculated. An empirical relationship between the nanoindentation hardness and uniaxial tensile yield stress was determined from diamond and HOPG references and found to lie between $K = 1.2 - 1.6$. This range was confirmed with a MD simulation of the nanoindentation of a particle of crosslinked PAH.

18

The results show that the hardness grows with the degree of crosslinking in the structure. There is a weak dependence on the size of the aromatic molecule used as the monomer, indicating that the hardness only depends on the degree of crosslinking and is not affected by H/C ratio and fringe length (values that depends on the starting monomer). Comparing our results with nanoindentation experiments, it was possible to estimate the degree of crosslinking in soot particles. Ethylene soot particles are found to have crosslinked densities between $2.1 - 3.0$ and diesel soot particles between $3.0 - 3.5$. The hardness of soot suggests that soot maturation involves crosslinking and carbonisation processes and that a 3D network of crosslinked PAH is present in mature soot.

Finally, our results show that particles with a degree of crosslinking between 0.0 and 1.5 are characterized by a high molecular mobility and their hardness values are consistent with the liquid-like behaviour that incipient soot particles show at high temperatures. The transition from the liquid-like behaviour of incipient soot particles to the solid state (mature soot) at flame temperatures may be related to an increase in the crosslinking density. However, nanoindentation experiments on incipient soot are required to explore this hypothesis.

We aim to follow up this study with further work on the impact of ring condensation and with more nanoindentation simulations.

Acknowledgements

References

Alfè, M., Apicella, B., Barbella, R., Rouzaud, J., Tregrossi, A. and Ciajolo, A. (2009), 'Structure–property relationship in nanostructures of young and mature soot in premixed flames', Proceedings of the Combustion Institute 32, 697–704.

Alfè, M., Apicella, B., Rouzaud, J., Tregrossi, A. and Ciajolo, A. (2010), 'The effect of temperature on soot properties in premixed methane flames', Combustion and Flame 157, 1959–1965.

Alfè, M., Apicella, B., Tregrossi, A. and Ciajolo, A. (2008), 'Identification of large polycyclic aromatic hydrocarbons in carbon particulates formed in a fuel-rich premixed ethylene flame', Carbon 46(15), 2059–2066.

Apicella, B., Pré, P., Alfè, M., Ciajolo, A., Gargiulo, V., Russo, C. and et al. (2015), 'Soot nanostructure evolution in premixed flames by High Resolution Electron Transmission Microscopy (HRTEM)', Proceedings of the Combustion Institute 35(2), 1895–1902.

Bhowmick, H. and Biswas, S. K. (2011), 'Relationship between physical structure and tribology of single soot particles generated by burning ethylene', Tribology Letters 44(2), 139–149.

Bhowmick, H., Majumdar, S. K. and Biswas, S. K. (2011), 'Dry tribology and nanomechanics of gaseous flame soot in comparison with carbon black and diesel soot', Proceedings of the Institution of Mechanical Engineers, Part C: Journal of Mechanical Engineering Science 226(2), 394–402.

Bond, T. C., Doherty, S. J., Fahey, D. W., Forster, P. M., Berntsen, T., Deangelo, B. J. and et al. (2013), 'Bounding the role of black carbon in the climate system: A scientific assessment', Journal of Geophysical Research Atmospheres 118(11), 5380–5552.

Botero, M. L., Chen, D., González-Calera, S., Jefferson, D. and Kraft, M. (2016), 'HRTEM

evaluation of soot particles produced by the non-premixed combustion of liquid fuels', Carbon 96, 459–473.

Brenner, D. W., Shenderova, O. A., Harrison, J. A., Stuart, S. J., Ni, B. and Sinnott, S. B. (2002), 'A second–generation reactive empirical bond order (REBO) potential energy expression for hydrocarbons', Journal of Physics: Condensed Matter 14(4), 783–802.

Buseck, P. R., Huang, B. and Keller, L. P. (1987), 'Electron microscope investigation of the structures of annealed carbons', Energy & Fuels 1(1), 105–110.

Chang, L., Zhou, C.-Y., Wen, L.-L., Li, J. and He, X. H. (2017), 'Molecular dynamics study of strain rate effects on tensile behavior of single crystal titanium nanowire', Computational Materials Science 128, 348–358.

Chen, S., Gong, X. G. and Wei, S. H. (2007), 'Superhard Pseudocubic BC2N Superlattices', Physical Review Letters 98(1), 015502.

Chung, S.-H. and Violi, A. (2011), 'Peri–condensed aromatics with aliphatic chains as key intermediates for the nucleation of aromatic hydrocarbons', Proceedings of the Combustion Institute 33(1), 693–700.

Ciajolo, A., Apicella, B., Barbella, R. and Tregrossi, A. (2000), 'Correlations of the spectroscopic properties with the chemical composition of flame–formed aromatic mixtures', Combustion Science and Technology 153, 19–32.

Commodo, M., De Falco, G., Bruno, A., Borriello, C., Minutolo, P. and D'Anna, A. (2015), 'Physicochemical evolution of nascent soot particles in a laminar premixed flame: from nucleation to early growth', Combustion and Flame 162(10), 3854–3863.

Commodo, M., Kaiser, K., De Falco, G., Minutolo, P., Shultz, F., D'Anna, A. and Gross, L. (2019), 'On the early stages of soot formation: Molecular structure elucidation by high-resolution atomic force microscopy', Combustion and Flame 205, 154–164.

D'Anna, A. (2009), 'Combustion–formed nanoparticles', Proceedings of the Combustion Institute 32, 593–613.

D'Anna, A., Violi, A., D'Alessio, A. and Sarofim, A. F. (2001), 'A Reaction pathway for nanoparticle formation in rich premixed flames', Combustion and Flame 127(1–2), 1995–2003.

Dastanpour, R., Momenimovahed, A., Thomson, K., Olfert, J. and Rogak, S. (2017), 'Variation of the optical properties of soot as a function of particle mass', Carbon 124, 201–211.

de Tomas, C., Suarez-Martinez, I. and Marks, N. A. (2018), 'Carbide-derived carbons for dense and tunable 3D graphene networks', Applied Physics Letters 112(25), 251907.

Dobbins, R. A., Fletcher, R. A. and Chang, H.-C. (1998), 'The evolution of soot precursor particles in a diffusion flame', Combustion and Flame 115(3), 285–298.

Donnet, J., Schultz, J. and Eckhardt, A. (1968), 'Etude de la microstructure d'un noir de carbone thermique', Carbon 6(6), 781–788.

Elvati, P. and Violi, A. (2013), 'Thermodynamics of poly-aromatic hydrocarbon clustering and the effects of substituted aliphatic chains', Proceedings of the Combustion Institute 34(1), 1837–1843.

Elvati, P. and Violi, A. (2018), 'Homo–dimerization of oxygenated polycyclic aromatic hydrocarbons under flame conditions', Fuel 222, 307–311.

Fan, X., Nose, K., Diao, D. and Yoshida, T. (2013), 'Nanoindentation behaviors of amorphous carbon films containing nanocrystalline graphite and diamond clusters prepared by radio frequency sputtering', Applied Surface Science 273, 816—823.

Flores, A., Calleja, F. J. B., Attenburrow, G. E. and Bassett, D. C. (2000), 'Microhardness studies of chain-extended pe: Iii. correlation with yield stress and elastic modulus', Polymer 41(14), 5431–5435.

Frenklach, M. (2002), 'Reaction mechanism of soot formation in flames', Physical Chemistry Chemical Physics 4(11), 2028–2037.

Frenklach, M. and Wang, H. (1991), 'Detailed modeling of soot particle nucleation and growth', Symposium (International) on Combustion 23(1), 1559–1566.

Heckman, F. A. and Harling, D. F. (1966), 'Progressive oxidation of selected particles of carbon black: further evidence for a new microstructural model', Rubber Chemistry and Technology 39(1), 1–13.

Heidenreich, R. D., Hess, W. M. and Ban, L. L. (1968), 'A test object and criteria for high resolution electron microscopy', Journal of Applied Crystallography 1(1), 1–19.

Herdman, J. D. and Miller, J. H. (2008), 'Intermolecular Potential Calculations for Polynuclear Aromatic Hydrocarbon Clusters', The Journal of Physical Chemistry A 112(28), 6249–6256.

Homann, K.-H. (1998), 'Fullerenes and soot formation – new pathways to large particles in flames', Angewandte Chemie International Edition 37(18), 2434–2451.

Iavarone, S., Pascazio, L., Sirignano, M., De Candia, A., Fierro, A., de Arcangelis, L. and D'Anna, A. (2017), 'Molecular dynamics simulations of incipient carbonaceous nanoparticle formation at flame conditions', Combustion Theory and Modelling 21(1), 49–61.

Ishiguro, T., Takatori, Y. and Akihama, K. (1997), 'Microstructure of diesel soot particles probed by electron microscopy: First observation of inner core and outer shell', Combustion and Flame 108(1-2), 231–234.

Iwashita, N. and Swain, M. V. (2002), 'Elasto-plastic deformation of glassy carbon by nano-indentation with spherical tipped indenters', Molecular Crystals and Liquid Crystals 386, 39–44.

Jenei, I. Z., Dassenoy, F., Epicier, T., Khajeh, A., Martini, A., Uy, D. and et al. (2018), 'Mechanical characterization of diesel soot nanoparticles: in situ compression in a transmission electron microscope and simulations', Nanotechnology 29, 085703.

Kholghy, M. R., Veshkini, A. and Thomson, M. J. (2016), 'The core-shell internal nanostructure of soot - A criterion to model soot maturity', Carbon 100, 508–536.

Landrigan, P. J., Fuller, R., Acosta, N. J. R., Adeyi, O., Arnold, R., Basu, N. N. and et al. (2017), 'The Lancet Commission on pollution and health', The Lancet. .

Lee, C., Wei, X., Kysar, J. and Hone, J. (2008), 'Measurement of the elastic properties and intrinsic strength of monolayer graphene', Science 321, 385–388.

Lewis, I. C. (1980), 'Thermal polymerization of aromatic hydrocarbons', Carbon 18(3), 191–196.

Li, Z., Zabihi, O., Wang, J., Li, Q., Wang, J., Lei, W. and Naebe, M. (2017), 'Hydrophilic pan based carbon nanofibres with improved graphitic structure and enhanced mechanical performance using ethylenediamine functionalized graphene', RSC Adv. 7, 2621–2628.

Mao, Q., Hou, D., Luo, K. H. and You, X. (2018), 'Dimerization of polycyclic aromatic hydrocarbon molecules and radicals under flame conditions', J. Phys. Chem. A 122, 8701−8708.

Mao, Q., van Duin, A. C. T. and Luo, K. H. (2017), 'Formation of incipient soot particles from polycyclic aromatic hydrocarbons: A ReaxFF molecular dynamics study', Carbon 121, 380–388.

Martinez, L., Andrade, R., Birgin, E. G. and Martínez, J. M. (2009), 'PACKMOL: A package for building initial configurations for molecular dynamics simulations', Journal of Computational Chemistry 30(13), 2157–2164.

Martyna, G. J., Klein, M. L. and Tuckerman, M. (1992), 'Nosè–Hoover chains: The canonical ensemble via continuous dynamics', The Journal of Chemical Physics 97(4), 2635–2643.

McConnell, J. R., Edwards, R., Kok, G. L., Flanner, M. G., Zender, C. S., Saltzman, E. S. and et al. (2007), '20th-century industrial black carbon emissions altered arctic climate forcing', Science 317(5843), 1381–1384.

Miller, J. H., Herdman, J. D., Green, C. D. O. and Webster, E. M. (2013), 'Experimental and computational determinations of optical band gaps for PAH and soot in a N2-diluted, ethylene/air non-premixed flame', Proceedings of the Combustion Institute 34(2), 3669–3675.

Minutolo, P., Gambi, G. and D'Alessio, A. (1996), 'The optical band gap model in the interpretation of the UV-visible absorption spectra of rich premixed flames', Symposium (International) on Combustion 26(1), 951–957.

Mitsuhashi, K., Ghosh, S. and Koibuchi, H. (2018), 'Mathematical modeling and simulations for large-strain j-shaped diagrams of soft biological materials', Polymers 10, 715.

O'Connor, T. C., Andzelm, J. and Robbins, M. O. (2015), 'AIREBO-M: A reactive model for hydrocarbons at extreme pressures', The Journal of Chemical Physics 142(2), 024903.

Parrinello, M. and Rahman, A. (1981), 'Polymorphic transitions in single crystals: A new molecular dynamics method', Journal of Applied Physics 52, 7182–7190.

Pascazio, L., Sirignano, M. and Anna, A. D. (2017), 'Simulating the morphology of clusters of polycyclic aromatic hydrocarbons : The influence of the intermolecular potential', Combustion and Flame 185, 53–62.

Patterson, J. R., Catledge, S. A., Vohra, Y. K., Akella, J. and Weir, S. T. (2000), 'Electrical and mechanical properties of C_{70} fullerene and graphite under high pressures studied using designer diamond anvils', Physical Review Letters 85(25), 5364–5367.

Plimpton, S. (1995), 'Fast parallel algorithms for short-range molecular dynamics', Journal of Computational Physics 117(1), 1–19.

Qomi, M. J. A., Ebrahimi, D., Bauchy, M., Pellenq, R. and Ulm, F.-J. (2017), 'Methodology for estimation of nanoscale hardness via atomistic simulations', Journal of Nanomechanics and Micromechanics 7(4), 04017011.

Ranganathan, R., Rokkam, S., Desai, T. and Keblinski, P. (2017), 'Generation of amorphous carbon models using liquid quench method: A reactive molecular dynamics study', Carbon 113, 87–99.

Rapacioli, M., Calvo, F., Spiegelman, F., Joblin, C. and Wales, D. J. (2005), 'Stacked clusters of polycyclic aromatic hydrocarbon molecules', The Journal of Physical Chemistry A 109(11), 2487–2497.

Rego, K. and Meunier, V. (2019), 'Carbon nanotube knots', AIP Advances 9, 025030.

Richter, A., Riesa, R., Smith, R., Henkel, M. and Wolf, B. (2000), 'Nanoindentation of diamond, graphite and fullerene films', Diamond and Related Materials 9, 170–184.

Russo, C., Alfè, M., Rouzaud, J. N., Stanzione, F., Tregrossi, A. and Ciajolo, A. (2013), 'Probing structures of soot formed in premixed flames of methane, ethylene and benzene', Proceedings of the Combustion Institute 34(1), 1885–1892.

Russo, C., Tregrossi, A. and Ciajolo, A. (2015), 'Dehydrogenation and growth of soot in premixed flames', Proc. Combust. Inst. 35, 1803–1809.

Schuetz, C. and Frenklach, M. (2002), 'Nucleation of soot: molecular dynamics simulations of pyrene dimerization', Proceedings of the Combustion Institute 29, 2307–2313.

Sediako, A. D., Soong, C., Howe, J. Y., Kholghy, M. R. and Thomson, M. J. (2017), 'Real-time observation of soot aggregate oxidation in an Environmental Transmission Electron Microscope', Proceedings of the Combustion Institute 36(1), 841–851.

Shahini, E., Taheri, K. K. and Taheri, A. K. (2017), 'An investigation on tensile properties of coiled carbon nanotubes using molecular dynamics simulation', Diamond and Related Materials 74, 154–163.

Stuart, S. J., Tutein, A. B. and Harrison, J. A. (2000), 'A reactive potential for hydrocarbons with intermolecular interactions', The Journal of Chemical Physics 112(14), 6472–6486.

Sweitzer, C. W. and Heller, G. L. (1956), 'The formation of carbon black in hydrocarbon flames', Rubber World 134, 855.

Tabor, D. (1951), The hardness of metals, Clarendon Press.

Takano, Y. and Koibuchi, H. (2017), 'J-shaped stress-strain diagram of collagen fibers: Frame tension of triangulated surfaces with fixed boundaries', Physical Review E 95, 042411.

Talyzin, A. V., Luzan, S. M., Leifer, K., Akhtar, S., Fetzer, J., Cataldo, F. and et al. (2011), 'Coronene fusion by heat treatment: Road to nanographenes', The Journal of Physical Chemistry C 115(27), 13207–13214.

Thompson, M. W., Dyatkin, B., Wang, H. W., Turner, C. H., Sang, X., Unocic, R. R. and et al. (2017), 'An atomistic carbide-derived carbon model generated using ReaxFF-based quenched Molecular Dynamics', C 4(3), 32.

Totton, T. S., Chakrabarti, D., Misquitta, A. J., Sander, M., Wales, D. J. and Kraft, M. (2010), 'Modelling the internal structure of nascent soot particles', Combustion and Flame 157(5), 909–914.

Totton, T. S., Misquitta, A. J. and Kraft, M. (2012), 'A quantitative study of the clustering of polycyclic aromatic hydrocarbons at high temperatures.', Physical Chemistry Chemical Physics 14(12), 4081–4094.

Tranter, R. S.and Klippenstein, S. J., Harding, L. B., Giri, B. R., Yang, X. and Kiefer, J. H. (2010), 'Experimental and theoretical investigation of the self-reaction of phenyl radicals', The Journal of Physical Chemistry A 114(32), 8240–8261.

Tregrossi, A. and Ciajolo, A. (2010), 'Spectral Signatures of Carbon Particulate Evolution in Methane Flames', Combustion Science and Technology 182(4-6), 683–691.

Unterreiner, B. V., Sierka, M. and Ahlrichs, R. (2004), 'Reaction pathways for growth of polycyclic aromatic hydrocarbons under combustion conditions, a DFT study', Physical Chemistry Chemical Physics 6(18), 4377–4384.

Violi, A., Kubota, A., Truong, T., Pitz, W., Westbrook, C. and Sarofim, A. (2002), 'A fully integrated kinetic monte carlo/molecular dynamics approach for the simulation of soot precursor growth', Proceedings of the Combustion Institute 29(2), 2343–2349.

Violi, A., Sarofim, A. F. and Voth, G. A. (2004), 'Kinetic Monte Carlo-molecular dynamics approach to model soot inception', Combustion Science and Technology 176(5-6), 991–1005.

Wang, H. (2011), 'Formation of nascent soot and other condensed-phase materials in flames', Proceedings of the Combustion Institute 33(1), 41–67.

Zhang, F. and Zhou, J. (2018), 'Molecular dynamics study of bimodal nanotwinned cu with a composite structure', Computational Materials Science 145, 60–67.

Zhang, H. B., You, X., Wang, H. and Law, C. K. (2014), 'Dimerization of polycyclic aromatic hydrocarbons in soot nucleation', The Journal of Physical Chemistry A 118(8), 1287–1292.

Zhao, B., Uchikawa, K. and Wang, H. (2007), 'A comparative study of nanoparticles in premixed flames by scanning mobility particle sizer, small angle neutron scattering, and transmission electron microscopy', Proceedings of the Combustion Institute 31, 851–860.

Zhao, H., Min, K. and Aluru, N. R. (2009), 'Size and Chirality Dependent Elastic Properties of Graphene Nanoribbons under Uniaxial Tension', Nano Letters 9(8), 3012–3015.

Zickler, G. A., Schöberl, T. and Paris, O. (2006), 'Mechanical properties of pyrolysed wood: a nanoindentation study', Philosophical Magazine 86(10), 1373–1386.

A Supplementary Data

A.1 Force field benchmark

The AIREBO potential has been previously benchmarked to reproduce structural and energetic properties of both gaseous and liquid hydrocarbons as well as diamond and graphite properties (Stuart et al., 2000). The AIREBO potential has also been extensively used to study the mechanical properties of carbon materials (Stuart et al., 2000; Zhao et al., 2009; O'Connor et al., 2015; Rego and Meunier, 2019). Its modified version, AIREBO-M, where the Lennard-Jones potential has been replaced with a Morse potential, has been further optimised to improve intermolecular steric repulsions, while preserving the ambient thermodynamics of the original potential. The potential was fit to experimental measurements of the layer spacing of graphite up to 14 GPa and first principles calculations of steric interactions between small alkanes (O'Connor et al., 2015). Although the AIREBO and AIREBO-M force fields have been benchmarked in literature, we did our own benchmarking to be sure that the force field can accurately reproduce the elastic properties of carbonaceous materials. The force field has been benchmarked in two ways.

Firstly, we calculated the bond dissociation energies using the AIREBO-M force field and using the dispersion corrected hybrid density functional M06-2X-D3/cc-pVTZ. Bond energies can be compared to the bond enthalpy benchmark values (NIST thermodynamic database) as the thermal correction is minimal at <1 kcal/mol. The biphenyl C-C bond energy has a benchmark value of -117.6 kcal/mol (Tranter et al., 2010); DFT calculations provided a value of -119.4 kcal/mol and AIREBO-M force field provided a value of -124.1 kcal/mol, showing in both cases a slight overestimation of the bond energy (+1.5% and +5.5% respectively). The binaphtalene C-C bond energy using AIREBO-M has a value of -125.9 kcal/mol, again showing a slight overestimation of the bond energy that has been found to be -120 kcal/mol from DFT calculations.

Secondly, and more importantly for the scope of this work, we checked the bond breaking process. We calculated the yield point and Young's modulus of graphene and diamond

as a benchmark using the same methodology reported in Section 4. The results agree with previous modelling studies and experimental values (Table 3), indicating that AIREBO-M provides the correct elastic response and that the Morse function used in this version of AIREBO ensures the correct asymmetric bond breaking potential surface. The calculated Young's modulus and yield stress values are always within 5% of the benchmark values as reported in Table 3. It is important to note that the values reported for diamond in Table 1 and 2 in the main text are an average between the ones computed for the $<100>$ and $<111>$ directions and the HOPG values in Table 1 and 2 are reported for the direction perpendicular to the aromatic plane.

[Figure 10 about here.]

[Table 3 about here.]

A.2 Effect of the strain rate

In order to investigate the effect of the strain rate on the tensile deformation, four different strain rates, i.e., $1 \cdot 10^{10}$ s^{-1} , $5 \cdot 10^9$ s^{-1}, $1 \cdot 10^9$ s^{-1} and $5 \cdot 10^8$ s^{-1} were considered. Figure 11 shows the stress-strain curves at different strain rates for the coronene system with $CL = 3.05$. We find that as the strain rate increases from $5 \cdot 10^8$ s^{-1} to $1 \cdot 10^{10}$ s^{-1}, the peak strength increases from 4.1 GPa to 5 GPa, while the initial slope of the stress-strain curve is insensitive to the strain rate. The strain at the peak also increases with increasing strain rate. Because of the small changes in the stress-strain curves upon decreasing the strain rate from $1 \cdot 10^9$ s^{-1} (green line) to $5 \cdot 10^8$ s^{-1} (blue line), we assume that the results will not considerably change when decreasing the strain rate below $5 \cdot 10^8$ s^{-1} and a strain rate of $5 \cdot 10^8$ s^{-1} was used for all the simulations.

[Figure 11 about here.]

A.3   Low CL systems

In Figure 3 (main text) the degree of crosslinking quickly increases, giving rise to structures with high degrees of crosslinking in the first picoseconds of the simulations due to the high number of reactive sites available in the crosslinking simulation. Here, fewer reactive sites were created in the simulation boxes by directly removing 1/4 (instead of 1/2 as in the main text) of the hydrogen atoms. The results are reported for the coronene system.

Figure 12 shows the CL versus time in both cases. As expected, systems with a lower CL were obtained starting from a lower number of reactive sites.

[Figure 12 about here.]

A.4   Effect of particle density

The density of the systems investigated in the main text is 1.5 g/cm^3. Soot density can reach values around 1.8 g/cm^3, so higher density systems have been also tested for comparison. The CL increases more quickly in the the crosslinking procedure for the systems with a higher density (Figure 13a and Figure 13b). Systems with the same CL but different densities provided the same yield stress and Young's modulus (slope of the linear part of the stress-strain curve before the yield stress point) values but they have different stress-strain curve shapes (Figure 13c and Figure 13d). The linear behaviour of the stress-strain curve of the high density systems indicates that all the new bonds are stretched at the same time at the start of the tensile test simulation.

[Figure 13 about here.]

When the density is lower the curve is J-shaped. The primary reason for these different elastic behaviours may be that the chains form random coils between the crosslink points within the 3D network when the density is lower. This depends on the larger distances between monomers that meet fewer reactive sites at the start of the simulation and form

more 'folded' networks. Moreover, the high density does not permit the molecules to arrange in stacks during the equilibration time so that they are more randomly distributed in the volume and form links in all directions. By changing the density we created different network designs but the yield stress and Young's modulus values were not affected, indicating that they depend exclusively on the CL of the structure.

A.5   Structural analysis

The aim of this study is to provide a link between the degree of crosslinking in the structure and mechanical properties. During the reactive MD simulations other reactions such as ring condensation, dehydrogenation and/or recombination of C–H bonds could occur. To be sure that only aliphatic crosslinking are forming in our system, the structures have been extensively checked at the end of the crosslinking MD simulation step before adding H atoms. Table 4 shows the percentage of broken bonds (C–C bond breakage and C–H bond breakage), the percentage of new bonds (crosslinks or other bonds) and the reaction occurrence in each system.

The proportion of bonds that break during the crosslinking procedure are always less than 0.5% and most of them are C–H bonds. A temperature of 1000 K ensures that a very small amount of the C–C bonds are broken. When a C–H breaks, a new reactive site is formed that can react and form other crosslinks in the structure and the H atoms can be involved in H migration or H abstractions reactions or remain in the system as a free radical. When a C-C bond breaks, ring opening reactions with a subsequent formation of aliphatic chains and/or new reactive sites as well as structural rearrangement can occur in the samples.

The main reaction detected in all the systems is the formation of crosslinks (>92% in all the considered systems). The second most common reaction is H abstraction by another reactive site that leads to the formation of a new reactive site (2-5%). The other reactions can be considered negligible. Ring condensations owing to H abstraction from a carbon

atom next to a reactive site were not observed.

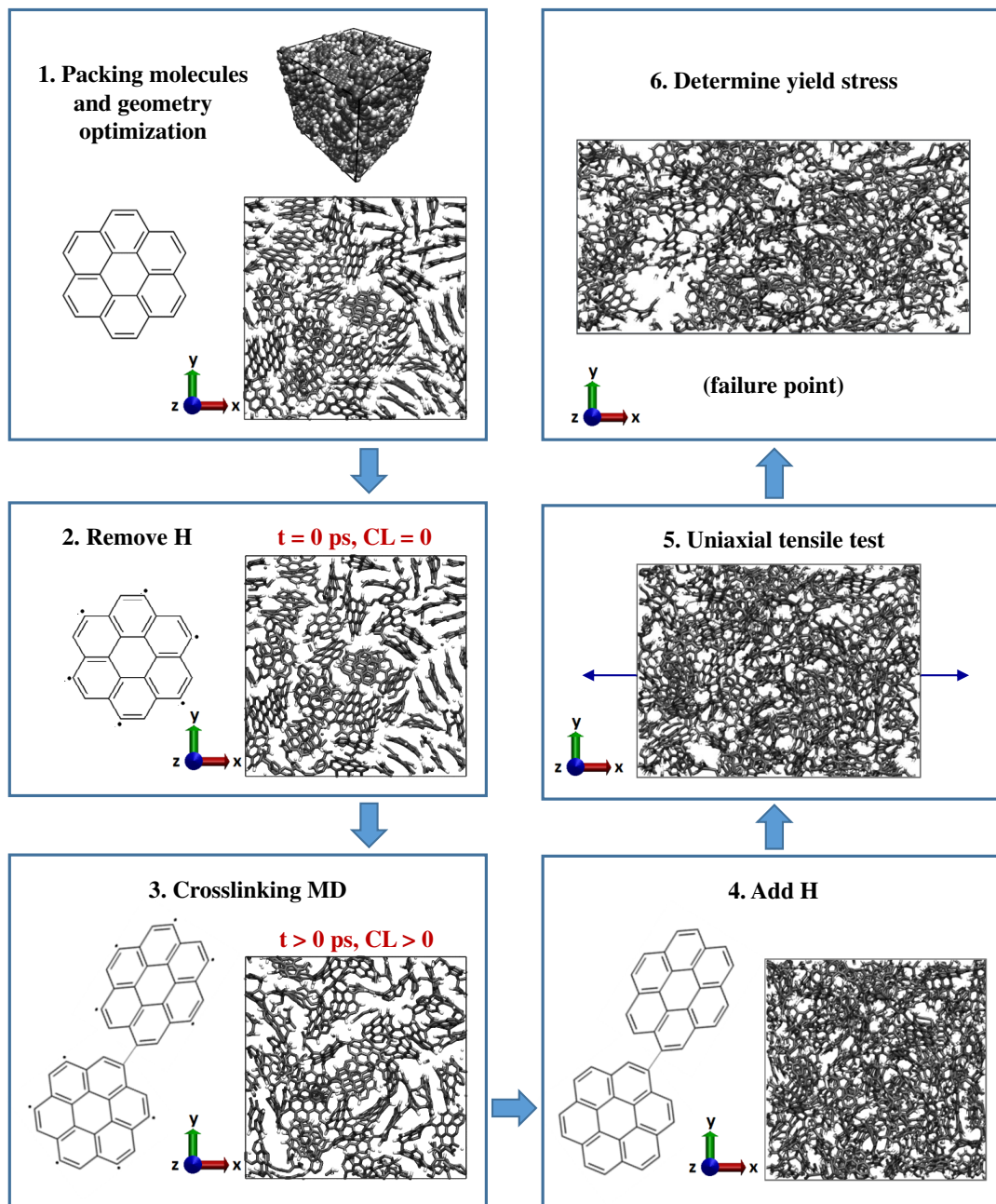[Table 4 about here.]

List of Figures

Figure 1: The steps involved in the crosslinking simulations: 1. the aromatic molecules are packed into the simulation box; 2. hydrogen atoms are removed from every second carbon atom around the rim of the molecule; 3. a reactive force field simulation is run and halted at different times to provide varying degrees of crosslinking; 4. hydrogen atoms are then added back to the sites that have not formed crosslinks; 5. and 6. the structure is uniaxially strained until failure. The images show slices of the simulation box of 10 Å thickness for step 1, 2 and 3 and of 20 Å thickness for step 4, 5 and 6.
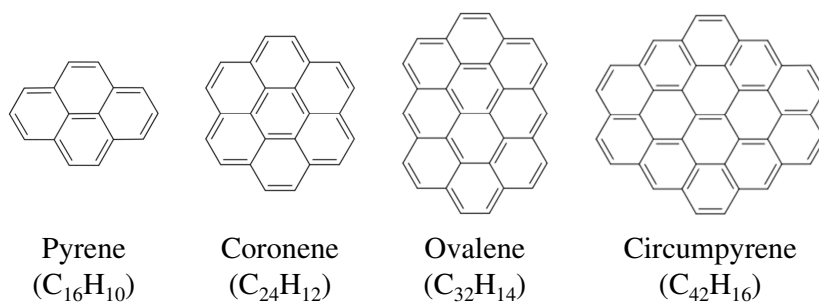
Figure 2: Molecular structure of the four investigated PAH monomers (pyrene, coronene, ovalene and circumpyrene).
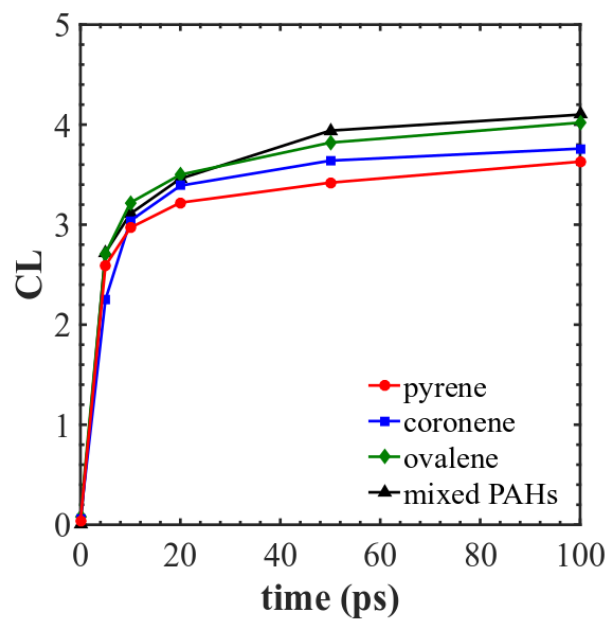
Figure 3: Degree of crosslinking (CL) as a function of MD time for pyrene, coronene and ovalene systems and for a heterogeneous system composed of 25% in number of each molecule type (mixed PAH in the figure)
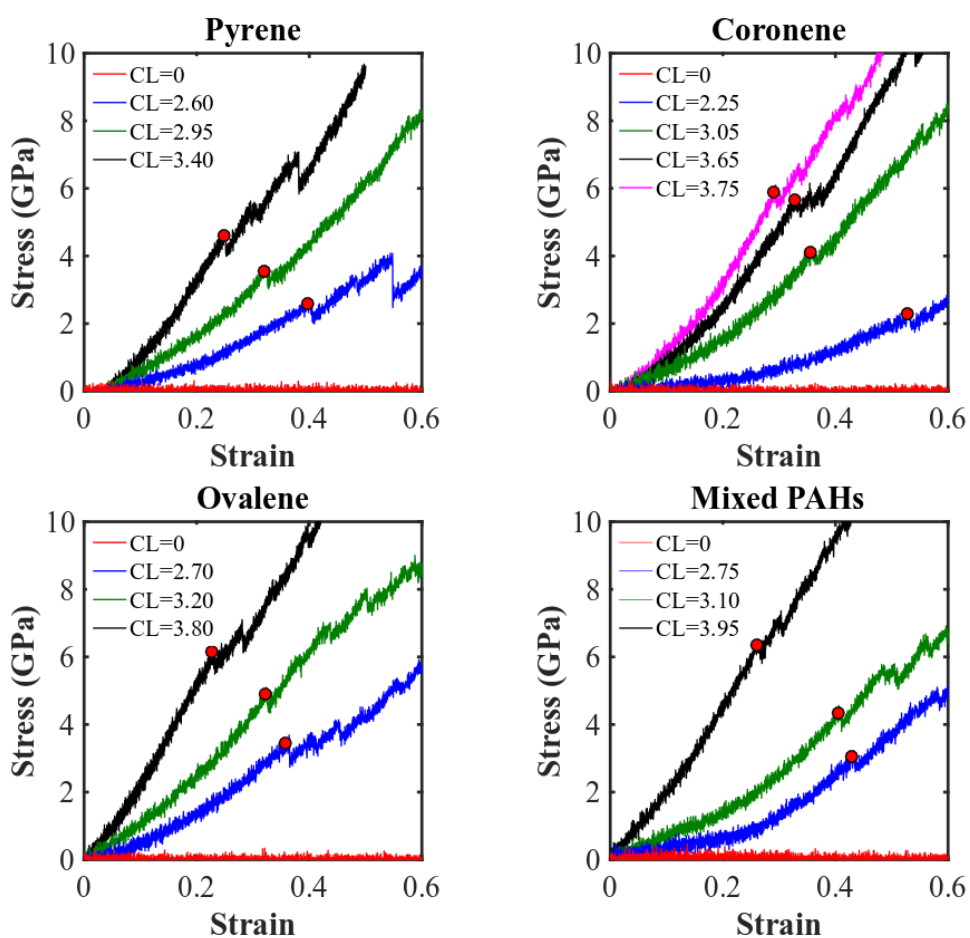
.

Figure 4: Stress-strain uniaxial tensile curves for pyrene, coronene and ovalene and for a heterogeneous system composed of 25% in number of each molecule type (mixed PAH in the figure) at varying degrees of crosslinking (CL). Red circles represent the yield point in each system.
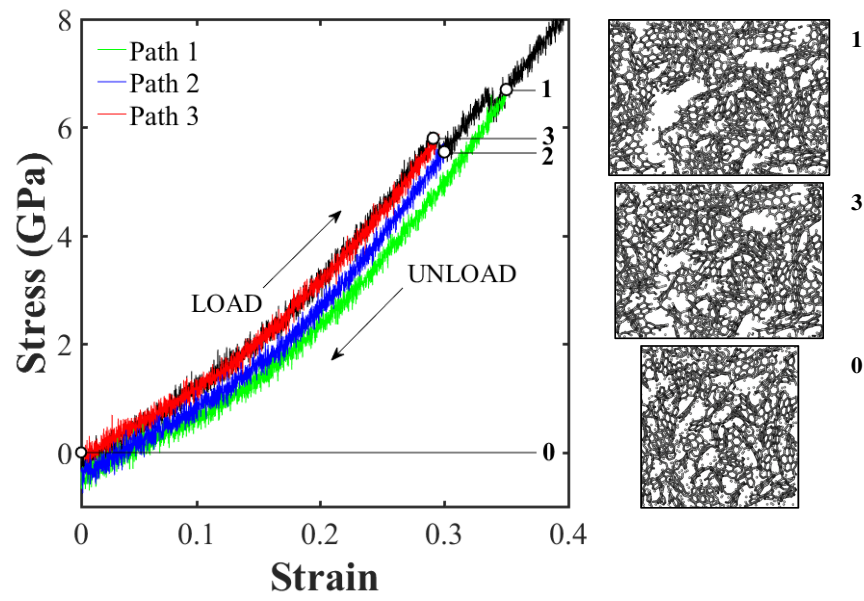
Figure 5: Stress-strain loading and unloading curves to determine yield stress for the coronene system with CL=3.75.
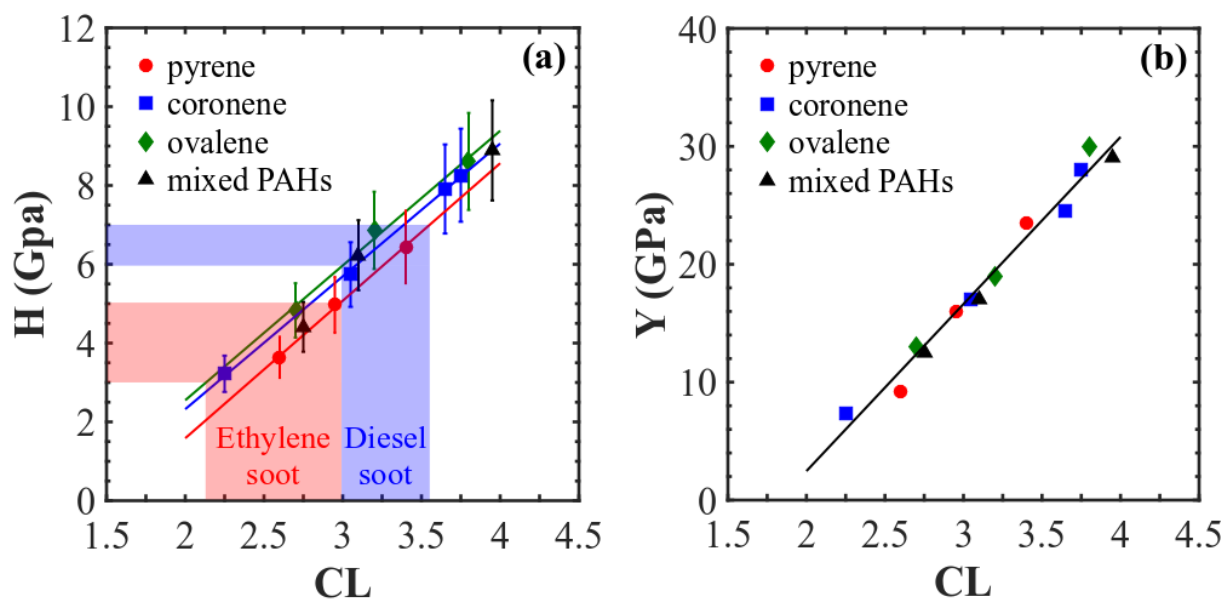
Figure 6: (a) Hardness (H) versus degree of crosslinking (CL) for the empirically determined values from the reactive force field uniaxial tensile tests using $K=1.4$ (with error bars showing $K=1.2$–1.6). The hardness values determined for diesel soot and ethylene soot are also shown for comparison (Bhowmick and Biswas, 2011; Bhowmick et al., 2011). (b) Young's modulus (Y) versus degree of crosslinking (CL).
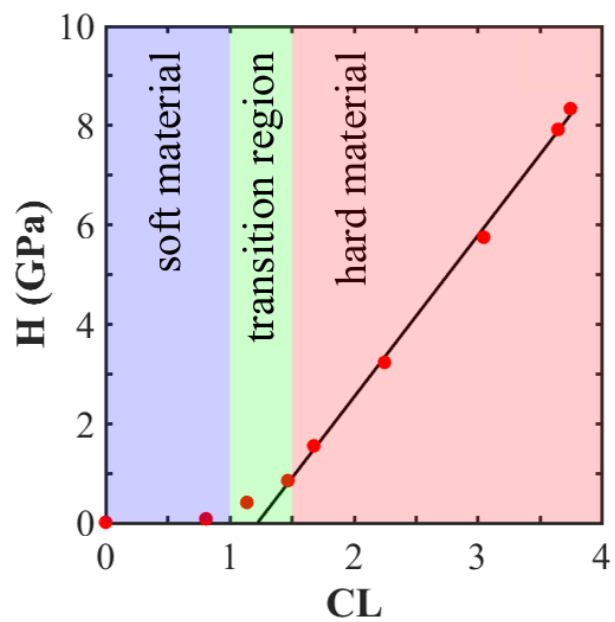
Figure 7: Hardness as function of degree of crosslinking (CL) for the coronene systems ($K = 1.4$).
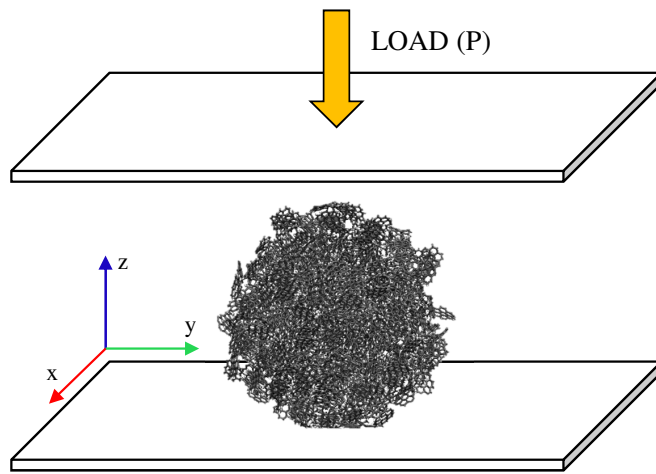
Figure 8: Molecular dynamics model of a particle of crosslinked coronene molecules for nanoindentation with a planar indenter.
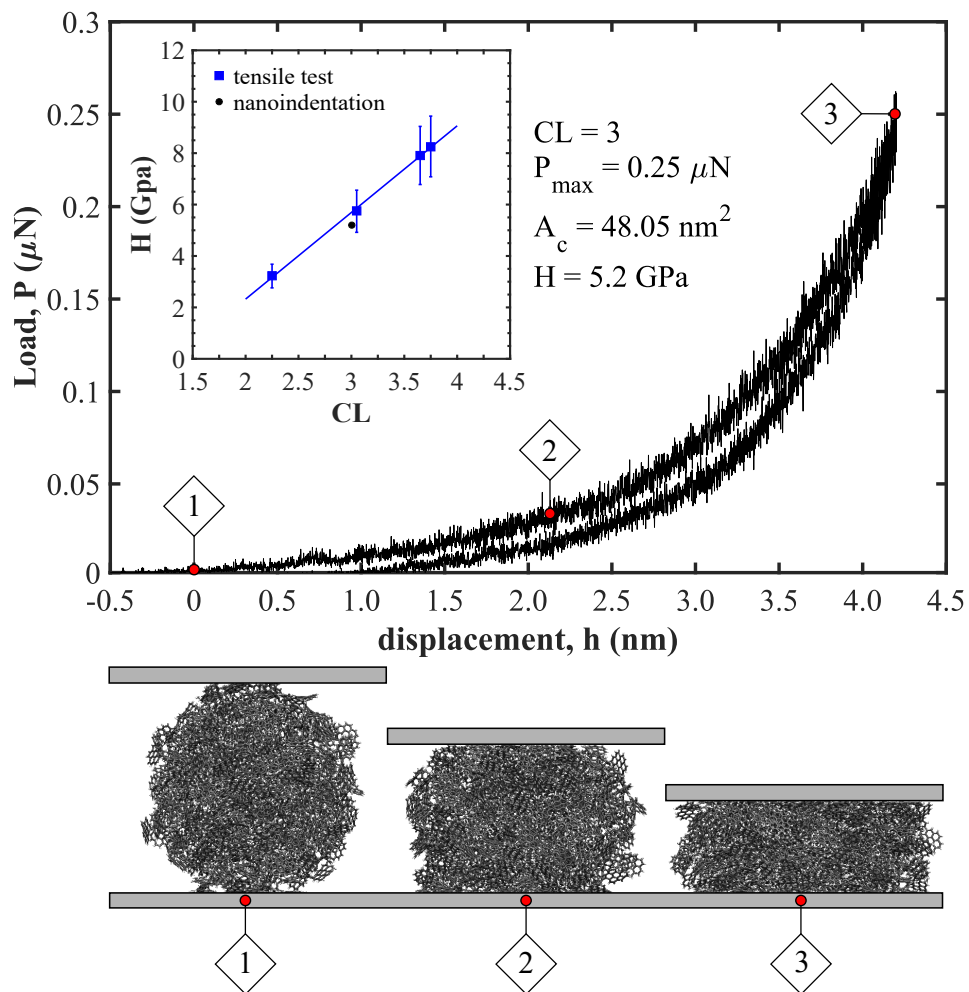
Figure 9: Load–displacement diagram and snapshots at different deformations (indentation depths) for a particle of crosslinked coronene molecules with CL=3. The insert shows a comparison between the hardness determined from the tensile test and the nanoindentation simulations.
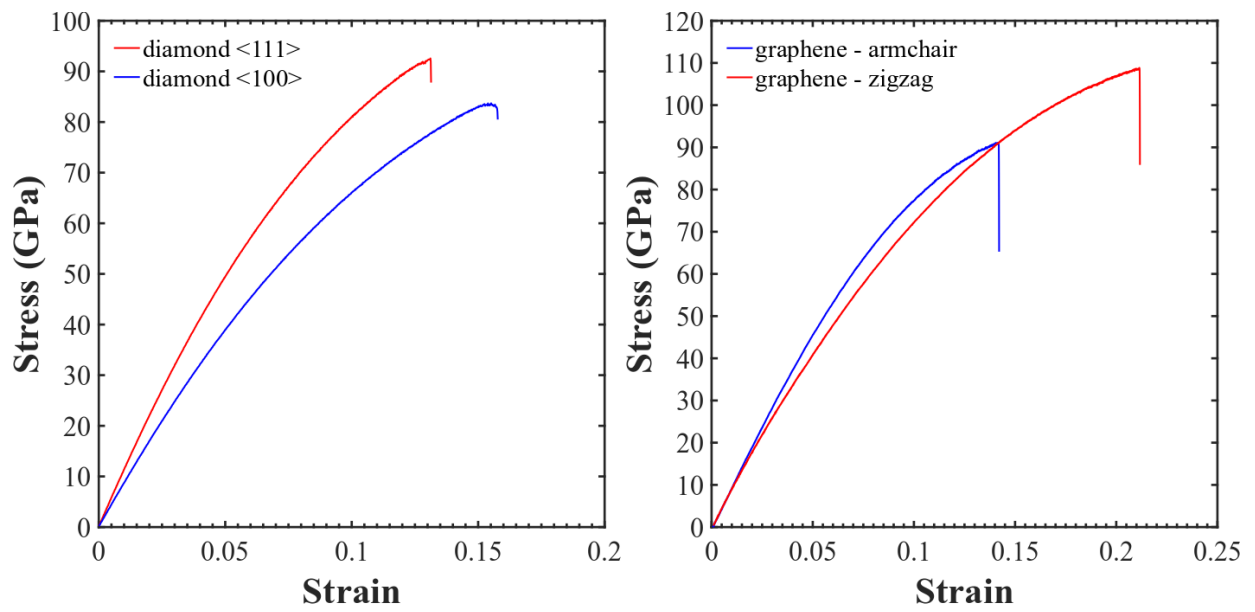
Figure 10: Stress-strain uniaxial tensile curves for diamond in the <111> and <100> directions (left) and for graphene in the armchair and zigzag directions (right).
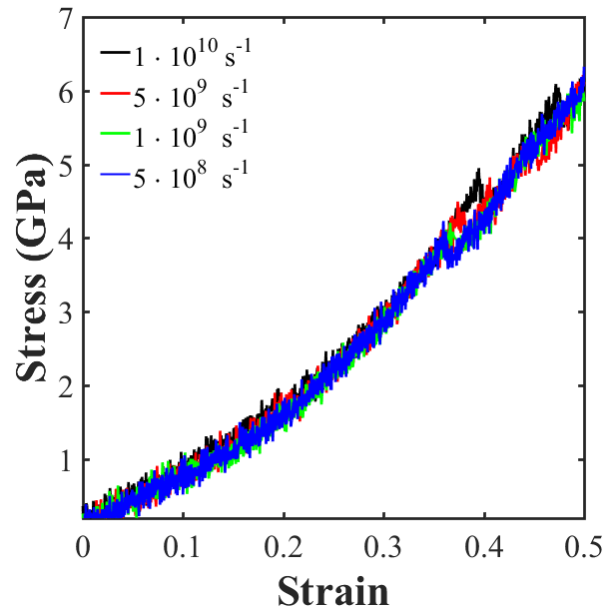
Figure 11: Stress-strain curves of tensile deformation at different strain rates for coronene system with $CL = 3.05$.
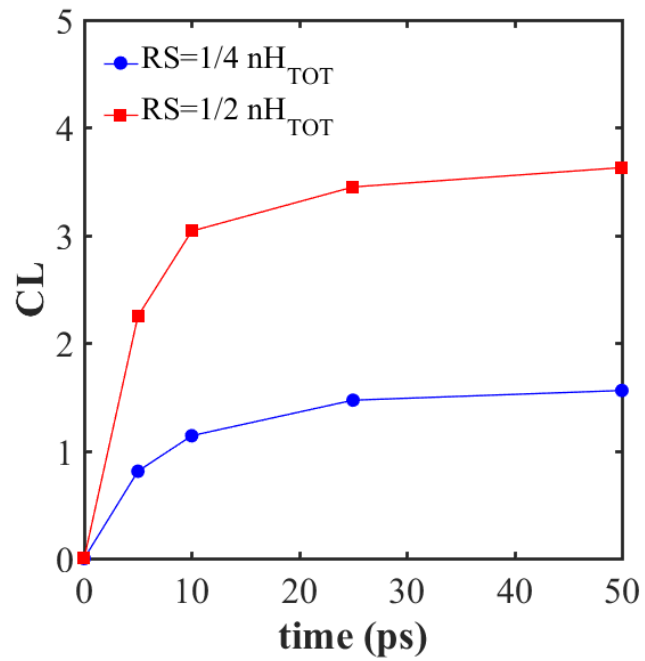
Figure 12: Degree of crosslinking (CL) as a function of MD time for coronene system starting from a different number of reactive sites (RS): the reactive sites are created by directly removing 1/4 of the starting hydrogen atoms (blue line) and 1/2 of hydrogen atoms (red line).
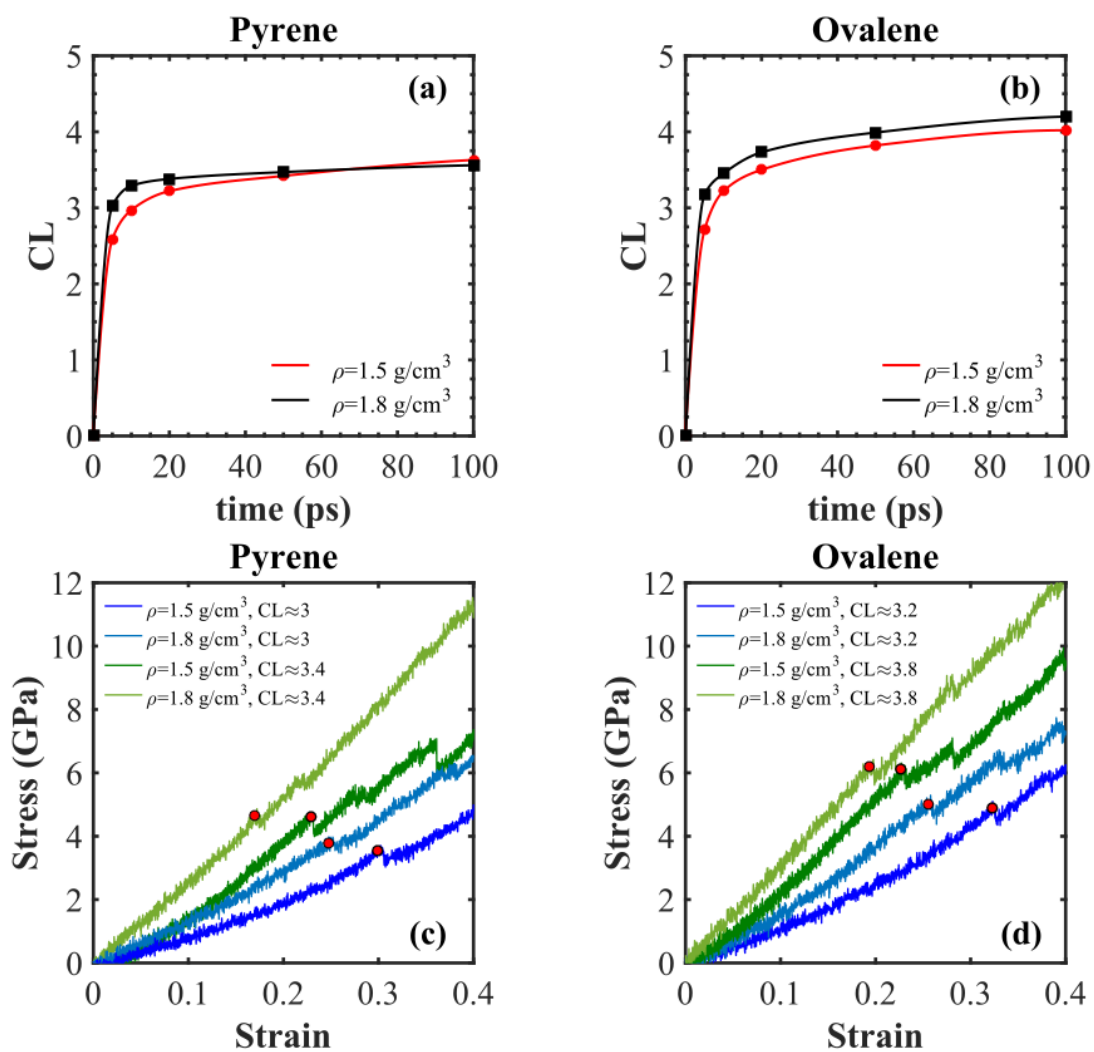
Figure 13: (a-b) Degree of crosslinking (CL) as a function of MD time and (c-d) Stress-strain curves of tensile deformation for low (1.5 g/cm^3) and high (1.8 g/cm^3) density systems at varying degrees of crosslinking (CL). Red circles represent the yield point in each system.

List of Tables

Table 1: Table of carbon-based materials hardness values from nanoindentation.

Material	Hardness (GPa)	Ref.
Nanocrystalline graphite	0.1–0.4	(Patterson et al., 2000)
HOPG	2.4	(Richter et al., 2000)
Carbon black	3–4	(Bhowmick and Biswas, 2011)
Ethylene soot	3–5	(Bhowmick and Biswas, 2011; Bhowmick et al., 2011)
Charcoal	3–5	(Zickler et al., 2006)
Diesel soot	6–7	(Bhowmick and Biswas, 2011)
Polymerised C_{70}	30	(Patterson et al., 2000)
Glassy carbon	30	(Iwashita and Swain, 2002)
Diamond	95-117	(Richter et al., 2000)

Table 2: Yield stress and hardness values for HOPG, diamond from nanoindentation by (Richter et al., 2000) and the investigated crosslinked PAH structures.

Material/PAH	Degree of crosslinking CL	H/C ratio	Yield stress σ_f (GPa)	Hardness H (GPa)	Conversion constant K	Young's modulus Y (GPa)
HOPG	–	–	1.5	2.4	1.6	–
Diamond	–	–	88	106	1.2	–
Pyrene	0.00	0.625	≈ 0	≈ 0	1.4	≈ 0
	2.60	0.46	2.60	3.64	1.4	9.5
	2.95	0.44	3.55	4.97	1.4	16
	3.40	0.41	4.60	6.44	1.4	23.5
Coronene	0.00	0.5	≈ 0	≈ 0	1.4	≈ 0
	2.25	0.40	2.30	3.22	1.4	7.5
	3.05	0.37	4.10	5.74	1.4	17
	3.65	0.35	5.65	7.91	1.4	24.5
	3.75	0.34	5.90	8.26	1.4	28
Ovalene	0.00	0.44	≈ 0	≈ 0	1.4	≈ 0
	2.70	0.35	3.45	4.83	1.4	13
	3.20	0.34	4.90	6.86	1.4	19
	3.80	0.32	6.15	8.61	1.4	30
Mixed PAH	0.00	0.46	≈ 0	≈ 0	1.4	≈ 0
	2.75	0.36	3.15	4.41	1.4	12.5
	3.10	0.35	4.45	6.23	1.4	17
	3.95	0.32	6.35	8.89	1.4	29

Table 3: Young's modulus, tensile yield stress and strain at which the yield stress occurs for diamond and graphite. The results are compared with previous calculations and experiments.

Structure	Direction	Yield Strain	Yield Stress (GPa)	Young's modulus (GPa)	Method	Ref.
Diamond	<111>	0.131	92.6	1151	MD	(this work)
		0.13 (+0.8%)	90.8 (+2%)	-	DFT	Chen et al. (2007)
		-	-	1137 (+1.2%)	exp.	Richter et al. (2000)
Diamond	<100>	0.155	83.4	897	MD	(this work)
		-	-	921 (-2.6%)	exp.	Richter et al. (2000)
Graphene	armchair	0.14	91.1	1051	MD	(this work)
		0.13 (+7.7%)	90 (+1.2%)	1010 (+4.1%)	MD	Zhao et al. (2009)
Graphene	zigzag	0.21	108.8	1012	MD	(this work)
		0.20 (+5.0%)	107 (+1.7%)	1010 (+0.2%)	MD	Zhao et al. (2009)
Graphene	in-plane	-	-	1000	exp.	Lee et al. (2008)

Table 4: (a) Percentage of conserved and broken bonds in relation to the number of bonds in the starting configuration and percentage of conserved and new bonds in relation to total number of bonds in each system. (b) Percentage of occurrence of each reaction type in relation to the total number of reaction events.

PAH	$C_{16}H_{10}$				$C_{24}H_{12}$					$C_{32}H_{14}$			
CL	0.00	2.60	2.95	3.40	0.00	2.25	3.05	3.65	3.75	0.00	2.70	3.20	3.80
(a) Bonds (%)													
Conserved bonds**	100	99.73	99.69	99.53	100	99.82	99.76	99.60	99.47	100	99.76	99.71	99.68
Broken bonds* C–C	0.00	0.04	0.04	0.04	0.00	0.04	0.04	0.06	0.07	0.00	0.09	0.09	0.09
C–H	0.00	0.22	0.27	0.43	0.00	0.14	0.20	0.34	0.46	0.00	0.15	0.20	0.23
Conserved bonds**	100	94.27	93.59	92.63	100	96.56	95.62	94.76	94.46	100	96.98	96.59	95.95
New bonds* crosslinks	0.00	5.52	6.14	7.01	0.00	3.30	4.19	4.94	5.14	0.00	4.40	4.44	4.81
other bonds	0.00	0.21	0.27	0.36	0.00	0.14	0.19	0.30	0.40	0.00	0.20	0.22	0.25
(b) Reactions (%)													
1) Formation of crosslinks	0.00	96.31	95.73	95.12	0.00	95.95	95.76	94.28	92.70	0.00	93.13	93.44	93.84
2) H abstraction	0.00	2.31	2.46	3.11	0.00	2.65	2.91	3.51	4.45	0.00	4.52	4.64	4.42
3) H migration	0.00	0.28	0.49	0.42	0.00	0.31	0.36	0.40	0.47	0.00	0.18	0.16	0.00
4) Formation of H*	0.00	0.00	0.00	0.00	0.00	0.00	0.00	0.00	0.00	0.00	0.36	0.00	0.00
5) Structural defect and/or ring opening	0.00	1.11	1.31	1.34	0.00	1.09	0.97	1.81	2.37	0.00	1.81	1.76	1.74
6) Cyclodehydrogenation	0.00	0.00	0.00	0.00	0.00	0.00	0.00	0.00	0.00	0.00	0.00	0.00	0.00

* in relation to the number of bonds in the starting configuration
** in relation to the number of bonds in the system